IEEE Access
Multidisciplinary | Rapid Review | Open Access Journal

Received September 12, 2018, accepted October 7, 2018, date of publication October 10, 2018, date of current version November 8, 2018.

Digital Object Identifier 10.1109/ACCESS.2018.2875090

Analysis of Inherent Characteristics, Load Sharing Characteristics, and Transportation Mechanical Response of a Transmission System in a Lunar Sampler and Its Experimental Verification

HONG XIAO, DEWEI TANG, ZONGQUAN DENG, CHUANYANG LI, AND SHENGYUAN JIANG
State Key Laboratory of Robotics and System, Harbin Institute of Technology, Harbin 15001, China

Corresponding author: Hong Xiao (number13_xh@163.com)

This work was supported in part by the technology research projects of the China Lunar Exploration under Project TY3Q20110001 and Project TY3Q20110005, in part by the National Nature Science Foundation of China under Grant 51105092 and Grant 61403106, in part by the 111 Project under Project B07018, and in part by the International Science and Technology Cooperation Program of China under Project 2014DFR50250.

ABSTRACT A rotary driving component is the power output unit of a lunar sampler. A planetary gear system is used as the transmission system. The lunar sampler is subjected to an extremely rigorous mechanical environment during transportation. In this paper, the time-varying meshing stiffness curves of planetary gears are calculated by the Shi Chuan method. A translational torsional dynamic model of a two-stage planetary gear system is established. Based on the Runge–Kutta method, a solution program is used to obtain the inherent characteristics of the transmission, and corresponding verification tests are performed. With respect to the transportation process (i.e., the stage between launch and landing), the dynamic response of the transmission is examined. With respect to adverse geological conditions, the load sharing characteristics of the transmission are calculated. The aforementioned investigations provide a theoretical basis for parameter setting and structural design of a lunar exploration project.

INDEX TERMS Lunar sampling, transmission system, dynamic analysis, load sharing characteristics, vibration test.

I. INTRODUCTION

The transportation process corresponds to the phase of launch to landing of the transmission is extremely harsh. Furthermore, given the complexity of the moon's surface, the transmission suffers from complex and irregular loads during the working process. In order to reduce the failure rate and improve working life and reliability, it is necessary to examine inherent characteristics, load sharing characteristics, and transportation mechanical response of the transmission.

The diagram of the transmission is shown in Figure 1. The transmission consists of two planetary gear systems, namely high-speed system (sun gear S^{I}, ring R^{I}, carrier C^{I}, planetary gears P_i^{I}) and low-speed system (sun gear S^{II}, ring R^{II}, carrier C^{II}, planetary gears P_i^{II}).

With respect to system modeling, Parker *et al.* [1] used finite element mechanics model to analyze the dynamic response of the helicopter planetary gear system in a certain speed and torque range. Sondkar and Kahraman [2] studied the double helical planetary gear drive system, and established a bending torsion axis pendulum coupling model of 18(N+3) degrees of freedom. Singh [3] established a three-dimensional finite element contact model, which was called GSAM model. Zhou *et al.* [4] proposed a new modeling method to research the vibroimpact characteristics of a planetary gear transmission system under high speed and lightly loaded conditions.

With respect to a model solution, Wang *et al.* [5] set up lumped parameter method and finite element method for dynamic performance of planetary gears. The solution method was given to analyze the force on the ring gear. Yavuz *et al.* [6] developed a nonlinear time-varying dynamic model of a drivetrain composed of a spiral bevel gear pair, shafts and bearings. Gear shafts were modeled by utilizing Timoshenko beam finite elements, and the mesh model of a spiral bevel gear pair was used to couple them.

With respect to inherent characteristics, Eritenel and Parker [7] have studied the inherent characteristics of helical gear planetary transmission system, and got

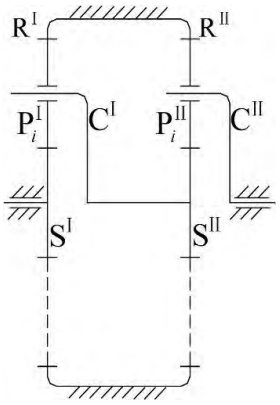

FIGURE 1. Transmission diagram.

the radial translation torsion pendulum mode, the axial translation torsion vibration mode and the planet wheel vibration mode. Guo and Parker [8] have studied the natural vibration characteristics of combined planetary gear transmission. Kiracofe and Parker [9] analyzed the characteristics in the combined planetary gear transmission system, and summed up the vibration mode as torsional vibration mode, lateral vibration mode and planetary gear vibration mode. Wu and Parker [10] analyzed the natural vibration characteristics of the uniform planetary gear transmission considering the internal gear elasticity, and summed up the vibration modes as torsional vibration mode, lateral vibration mode, planetary gear vibration mode and pure inner gear ring vibration mode. Guo and Parker [11] studied the inherent vibration sensitivity of composite planetary gear transmission system.

With respect to dynamic characteristics, Wang *et al.* [12] established a flexible multi-body dynamics analysis model for the multistage system of wind power planetary transmission gearbox, and studied the system dynamic characteristics. Zhou *et al.* [13] set up a sixteen degree of freedom lumped parameter dynamic model and used Runge-Kutta method to study the dynamic behavior of spur gear rotor system. Ambarisha and Parker [14] and Parker and Lin [15] have solved the relationship between the meshing phase, the time varying meshing stiffness and the equivalent error on the meshing line.

With respect to load sharing characteristics, Montestruc [16] summarized the research on load sharing characteristics of planetary gear trains. Bodas and Kahraman [17] used two dimensional finite element contact model to study the relationship between the planetary gear manufacturing error and the static load sharing coefficient of the system. Ligata *et al.* [18] proposed a discrete model for calculating the static inhomogeneous coefficient, and derived a formula for calculating the static unequal load factor of four sets of planetary gears.

With respect to experiments, Hong *et al.* [19] integrated the analytical model, a denoising algorithm, and frequency domain indicators into one synergistic system to detect and identify the damaged gear teeth in the planetary gearboxes. A planetary gearbox test rig validated the dynamic simulations and the experimental data. Shuiqing *et al.* [20] proposed a method based on the multiscale chirplet path pursuit (MSCPP) and the linear canonical transform (LCT), and the method has been applied to diagnose the gear fault in the variable speed condition for the first time. Simulations and experimental evaluations were provided to verify the effectiveness of the proposed method. Yu *et al.* [21] proposed a new dynamic model of a cylindrical gear pair with localized tooth spalling defects. Experimental vibration responses of several 1:1 ratio spur gear pair sets with different dimensions of spalling defects were measured to compare with the simulated results. The results validated the superiority of the proposed model against previous similar models.

In this study, a translational torsional dynamic model of a transmission system is established. Based on Shi Chuan method, the internal and external time-varying meshing stiffness are accurately calculated. Based on the Runge–Kutta method, a solution program is used to obtain the inherent characteristics of the transmission. Thus, the mechanical environment of the delivery stage is analyzed, and the dynamic response of the transmission is calculated. The static and dynamic load sharing coefficients of the transmission are analyzed.

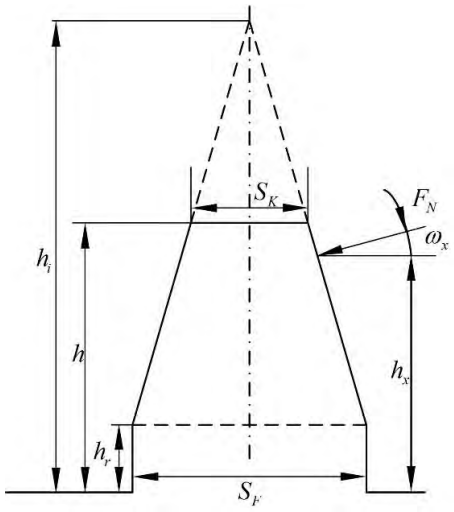

FIGURE 2. Approximate tooth shape.

II. CALCULATION OF TIME-VARYING MESH STIFFNESS BASED ON SHI CHUAN METHOD

In an engagement cycle of a pair of gears, the phenomenon of single-tooth meshing and double-tooth meshing is observed. The generation of time-varying meshing stiffness occurs. In this study, Shi Chuan method is used to calculate internal and external time-varying meshing stiffness. The method simplifies a gear into a cantilever beam composed of a trapezoid and rectangle as shown in Figure 2. ISO 30° dangerous section is shown in Figure 3.

The deformation of a single tooth along the meshing line direction in a meshing tool pair is as follows:

$$\delta = \delta_{Br} + \delta_{Bt} + \delta_s + \delta_G + \delta_p \tag{1}$$

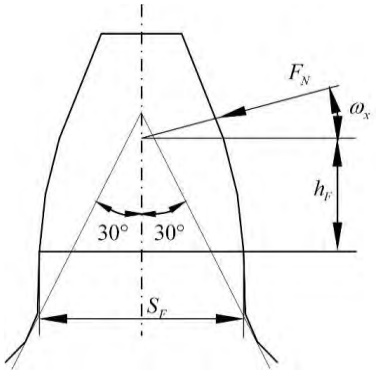

FIGURE 3. ISO 30° dangerous section.

Bending deformation of the rectangular section is as follows:

$$\delta_{Br} = \frac{12F_N \cos^2 \omega_x}{Ebs_F^3}\left[h_x h_r (h_x - h_r) + \frac{h_r^3}{3}\right] \tag{2}$$

Bending deformation of the trapezoidal part is as follows:

$$\delta_{Bt} = \frac{6F_N \cos^2 \omega_x}{Ebs_F^3}\left[\frac{h_i - h_x}{h_i - h_r}\left(4 - \frac{h_i - h_x}{h_i - h_r}\right) - 2\ln\frac{h_i - h_x}{h_i - h_r} - 3\right](h_i - h_r)^3 \tag{3}$$

$$h_i = \frac{hS_F - h_r S_k}{S_F - S_K} \tag{4}$$

Deformation produced by the shear force is as follows:

$$\delta_s = \frac{2(1+\nu)F_N \cos^2 \omega_x^2}{EbsF}\left[h_r + (h_i - h_r)\ln\frac{h_i - h_r}{h_i - h_x}\right] \tag{5}$$

Deformation produced by the base part tilt is as follows:

$$\delta_G = \frac{24F_N h_x^2 \cos^2 \omega_x}{\pi Ebs_F^2} \tag{6}$$

Deformation produced by gear tooth surface contact is as follows:

$$\delta_p = \frac{4F_N(1-\nu^2)}{\pi Eb} \tag{7}$$

Therefore, the time-varying meshing stiffness is calculated by the deformation amount in the direction of the meshing line. The time-varying meshing stiffness curves are shown in Figures 4–7.

III. ESTABLISH OF THE TRANSMISSION DYNAMIC MODEL

A. DYNAMIC MODEL OF TRANSMISSION

The dynamic model of the transmission system is shown in Figure 8. The levels of high-speed and low-speed exhibit the same structural form, and thus, the high-speed level is considered as an example in the following analysis. Specifically, x_s^{I}, y_s^{I}, and u_s^{I} denote the lateral, longitudinal, and torsional displacements, respectively, of the sun gear; ξ_i^{I}, η_i^{I}, and u_i^{I} denote the lateral, longitudinal, and torsional displacements, respectively, of the planetary gear; x_r^{I}, y_r^{I}, and u_r^{I} denote the lateral, longitudinal, and torsional displacements, respectively, of the ring gear; and x_c^{I}, y_c^{I}, and u_c^{I}

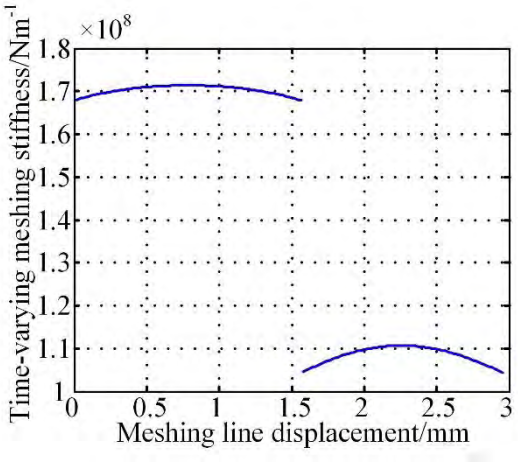

FIGURE 4. Curves of high-speed external meshing.

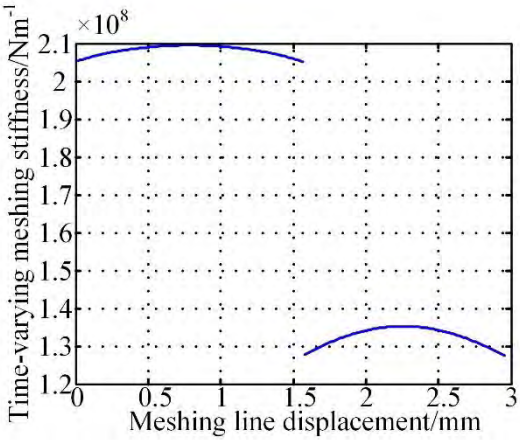

FIGURE 5. Curves of low-speed external meshing.

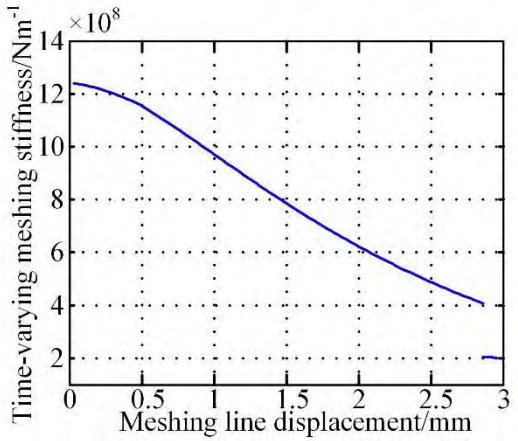

FIGURE 6. Curves of high-speed internal meshing.

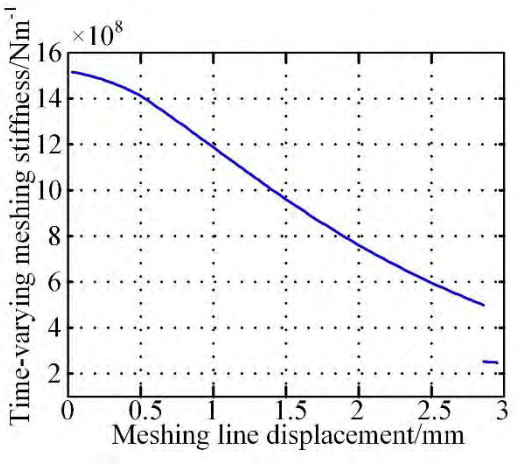

FIGURE 7. Curves of low-speed internal meshing.

denote the lateral, longitudinal, and torsional displacements, respectively, of the carrier. Stiffness includes gear mesh stiffness, bearing stiffness, and torsion stiffness. Specifically, k_{ri}^{I} denotes the mesh stiffness of the inner gear and planetary gear; k_{si}^{I} denotes the mesh stiffness of the sun gear and the planetary gear. k_{sx}^{I}, k_{sy}^{I} and k_{su}^{I} denote the bearing stiffness of the sun gear; k_{rx}^{I}, k_{ry}^{I}, and k_{ru}^{I} denote the bearing stiffness of the ring gear; $k_{pi\xi}^{\mathrm{I}}$ and $k_{pi\eta}^{\mathrm{I}}$ denote the bearing stiffness of the planetary gear; and $k_{c^{\mathrm{I}}s^{\mathrm{II}}}$ denotes the torsional stiffness between the carrier in the high-speed level and the sun gear in the low-speed level.

In Figure 8, the direction of the planetary gear with respect to the sun gear or inner gear is positive. Therefore, the elastic deformation on the meshing line of planetary gear and sun gear is as follows:

$$\begin{cases} \delta_{si} = x_s \sin\psi_{si} - y_s \cos\psi_{si} - u_s + \xi_i \sin\alpha_s + \eta_i \cos\alpha_s - u_i \\ \psi_{si} = \psi_i - \alpha_s \end{cases} \tag{8}$$

The elastic deformation on the meshing line of planetary gear and inner gear is as follows:

$$\begin{cases} \delta_{ri} = x_r \sin\psi_{ri} - y_r \cos\psi_{ri} - u_r - \xi_i \sin\alpha_r + \eta_i \cos\alpha_r + u_i \\ \psi_{ri} = \psi_i + \alpha_r \end{cases} \tag{9}$$

The elastic deformation of the planet gear relative to the carrier in two coordinate axes is as follows:

$$\begin{cases} \delta_{ir} = \xi_i - x_c \cos\psi_i - y_c \sin\psi_i \\ \delta_{it} = \eta_i + x_c \sin\psi_i - y_c \cos\psi_i - u_c \end{cases} \tag{10}$$

B. FORCE ANALYSIS OF EACH COMPONENT IN THE TRANSMISSON SYSTEM

Based on the force condition of the internal components in the transmission, the motion differential equations of the sun gear S^{I} are as follows:

$$\begin{cases} m_s^{\mathrm{I}}\ddot{x}_s^{\mathrm{I}} + \sum_{i=1}^{3}\left(c_{si}^{\mathrm{I}}\dot{\delta}_{si}^{\mathrm{I}} + k_{si}^{\mathrm{I}}\delta_{si}^{\mathrm{I}}\right)\sin\psi_{si}^{\mathrm{I}} + c_{sx}^{\mathrm{I}}\dot{x}_s^{\mathrm{I}} + k_{sx}^{\mathrm{I}}x_s^{\mathrm{I}} = 0 \\ m_s^{\mathrm{I}}\ddot{y}_s^{\mathrm{I}} - \sum_{i=1}^{3}\left(c_{si}^{\mathrm{I}}\dot{\delta}_{si}^{\mathrm{I}} + k_{si}^{\mathrm{I}}\delta_{si}^{\mathrm{I}}\right)\cos\psi_{si}^{\mathrm{I}} + c_{sy}^{\mathrm{I}}\dot{y}_s^{\mathrm{I}} + k_{sy}^{\mathrm{I}}y_s^{\mathrm{I}} = 0 \\ \left[I_s^{\mathrm{I}}/(r_s^{\mathrm{I}})^2\right]\ddot{u}_s^{\mathrm{I}} - \sum_{i=1}^{3}\left(c_{si}^{\mathrm{I}}\dot{\delta}_{si}^{\mathrm{I}} + k_{si}^{\mathrm{I}}\delta_{si}^{\mathrm{I}}\right) + c_{su}^{\mathrm{I}}\dot{u}_s^{\mathrm{I}} + k_{su}^{\mathrm{I}}u_s^{\mathrm{I}} \\ \qquad = T_s^{\mathrm{I}}/r_s^{\mathrm{I}} \end{cases} \tag{11}$$

The motion differential equations of the inner gear R^{I} are as follows:

$$\begin{cases} m_r^{\mathrm{I}}\ddot{x}_r^{\mathrm{I}} + \sum_{i=1}^{3}\left(c_{ri}^{\mathrm{I}}\dot{\delta}_{ri}^{\mathrm{I}} + k_{ri}^{\mathrm{I}}\delta_{ri}^{\mathrm{I}}\right)\sin\psi_{ri}^{\mathrm{I}} + c_{rx}^{\mathrm{I}}\dot{x}_r^{\mathrm{I}} + k_{rx}^{\mathrm{I}}x_r^{\mathrm{I}} = 0 \\ m_r^{\mathrm{I}}\ddot{y}_r^{\mathrm{I}} - \sum_{i=1}^{3}\left(c_{ri}^{\mathrm{I}}\dot{\delta}_{ri}^{\mathrm{I}} + k_{ri}^{\mathrm{I}}\delta_{ri}^{\mathrm{I}}\right)\cos\psi_{ri}^{\mathrm{I}} + c_{ry}^{\mathrm{I}}\dot{y}_r^{\mathrm{I}} + k_{ry}^{\mathrm{I}}y_r^{\mathrm{I}} = 0 \\ \left[I_r^{\mathrm{I}}/(r_r^{\mathrm{I}})^2\right]\ddot{u}_r^{\mathrm{I}} - \sum_{i=1}^{3}\left(c_{ri}^{\mathrm{I}}\dot{\delta}_{ri}^{\mathrm{I}} + k_{ri}^{\mathrm{I}}\delta_{ri}^{\mathrm{I}}\right) + c_{ru}^{\mathrm{I}}\dot{u}_r^{\mathrm{I}} + k_{ru}^{\mathrm{I}}u_r^{\mathrm{I}} = 0 \end{cases} \tag{12}$$

The motion differential equations of the carrier C^{I} are as follows:

$$\begin{cases} m_c^{\mathrm{I}}\ddot{x}_c^{\mathrm{I}} + c_{cx}^{\mathrm{I}}\dot{x}_c^{\mathrm{I}} + k_{cx}^{\mathrm{I}}x_c^{\mathrm{I}} \\ \qquad = \sum_{i=1}^{3}\left[k_{pi\xi}^{\mathrm{I}}\delta_{ir}^{\mathrm{I}}\cos\psi_i^{\mathrm{I}} - k_{pi\eta}^{\mathrm{I}}\delta_{it}^{\mathrm{I}}\sin\psi_i^{\mathrm{I}} + c_{pi\xi}^{\mathrm{I}}\dot{\delta}_{ir}^{\mathrm{I}}\cos\psi_i^{\mathrm{I}} - c_{pi\eta}^{\mathrm{I}}\dot{\delta}_{it}^{\mathrm{I}}\sin\psi_i^{\mathrm{I}}\right] \\ m_c^{\mathrm{I}}\ddot{y}_c^{\mathrm{I}} + c_{cy}^{\mathrm{I}}\dot{y}_c^{\mathrm{I}} + k_{cy}^{\mathrm{I}}y_c^{\mathrm{I}} \\ \qquad = \sum_{i=1}^{3}\left[k_{pi\xi}^{\mathrm{I}}\delta_{ir}^{\mathrm{I}}\sin\psi_i^{\mathrm{I}} + k_{pi\eta}^{\mathrm{I}}\delta_{it}^{\mathrm{I}}\cos\psi_i^{\mathrm{I}} + c_{pi\xi}^{\mathrm{I}}\dot{\delta}_{ir}^{\mathrm{I}}\sin\psi_i^{\mathrm{I}} + c_{pi\eta}^{\mathrm{I}}\dot{\delta}_{it}^{\mathrm{I}}\cos\psi_i^{\mathrm{I}}\right] \\ \left[I_c^{\mathrm{I}}/(r_c^{\mathrm{I}})^2\right]\ddot{u}_c^{\mathrm{I}} - \sum_{i=1}^{3}(c_{pi\xi}^{\mathrm{I}}\dot{\delta}_{it}^{\mathrm{I}} + k_{pi\xi}^{\mathrm{I}}\delta_{it}^{\mathrm{I}}) + c_{cu}^{\mathrm{I}}\dot{u}_c^{\mathrm{I}} + k_{cu}^{\mathrm{I}}u_c^{\mathrm{I}} \\ \qquad = -\frac{k_{c^{\mathrm{I}}s^{\mathrm{II}}}}{r_c^{\mathrm{I}}}\left(\frac{u_c^{\mathrm{I}}}{r_c^{\mathrm{I}}} - \frac{u_s^{\mathrm{II}}}{r_s^{\mathrm{II}}}\right) - \frac{c_{c^{\mathrm{I}}s^{\mathrm{II}}}}{r_c^{\mathrm{I}}}\left(\frac{\dot{u}_c^{\mathrm{I}}}{r_c^{\mathrm{I}}} - \frac{\dot{u}_s^{\mathrm{II}}}{r_s^{\mathrm{II}}}\right) \end{cases} \tag{13}$$

The motion differential equations of the planetary gear $\mathrm{P}_i^{\mathrm{I}}$ are as follows:

$$\begin{cases} m_p^{\mathrm{I}}\left(\ddot{\xi}_p^{\mathrm{I}} - 2\omega_c^{\mathrm{I}}\dot{\eta}_p^{\mathrm{I}} - \omega_c^{\mathrm{I}2}\xi_p^{\mathrm{I}}\right) + \left(c_{si}^{\mathrm{I}}\dot{\delta}_{si}^{\mathrm{I}} + k_{si}^{\mathrm{I}}\delta_{si}^{\mathrm{I}}\right)\sin\alpha_{si}^{\mathrm{I}} \\ \qquad = \left(c_{ri}^{\mathrm{I}}\dot{\delta}_{ri}^{\mathrm{I}} + k_{ri}^{\mathrm{I}}\delta_{ri}^{\mathrm{I}}\right)\sin\alpha_{ri}^{\mathrm{I}} - \left(c_{pi\xi}^{\mathrm{I}}\dot{\delta}_{ir}^{\mathrm{I}} + k_{pi\xi}^{\mathrm{I}}\delta_{ir}^{\mathrm{I}}\right) \\ m_p^{\mathrm{I}}\left(\ddot{\eta}_p^{\mathrm{I}} + 2\omega_c^{\mathrm{I}}\dot{\xi}_p^{\mathrm{I}} - \omega_c^{\mathrm{I}2}\eta_p^{\mathrm{I}}\right) + \left(c_{si}^{\mathrm{I}}\dot{\delta}_{si}^{\mathrm{I}} + k_{si}^{\mathrm{I}}\delta_{si}^{\mathrm{I}}\right)\cos\alpha_{si}^{\mathrm{I}} \\ \qquad - \left(c_{ri}^{\mathrm{I}}\dot{\delta}_{ri}^{\mathrm{I}} + k_{ri}^{\mathrm{I}}\delta_{ri}^{\mathrm{I}}\right)\cos\alpha_{ri}^{\mathrm{I}} - \left(c_{pi\eta}^{\mathrm{I}}\dot{\delta}_{it}^{\mathrm{I}} + k_{pi\eta}^{\mathrm{I}}\delta_{it}^{\mathrm{I}}\right) = 0 \\ \left[I_p^{\mathrm{I}}/(r_p^{\mathrm{I}})^2\right]\ddot{u}_p^{\mathrm{I}} + c_{piu}^{\mathrm{I}}\dot{u}_p^{\mathrm{I}} + k_{piu}^{\mathrm{I}}u_p^{\mathrm{I}} \\ \qquad = (c_{si}^{\mathrm{I}}\dot{\delta}_{si}^{\mathrm{I}} + k_{si}^{\mathrm{I}}\delta_{si}^{\mathrm{I}}) - (c_{ri}^{\mathrm{I}}\dot{\delta}_{ri}^{\mathrm{I}} + k_{ri}^{\mathrm{I}}\delta_{ri}^{\mathrm{I}}) \end{cases} \tag{14}$$

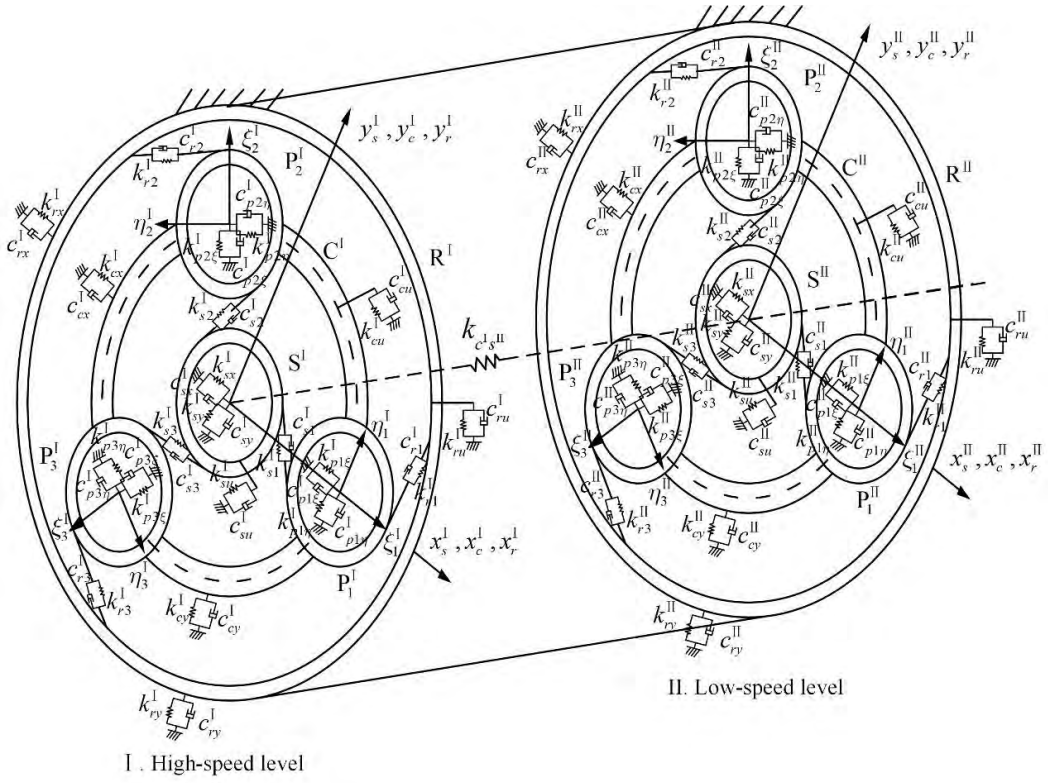

FIGURE 8. Dynamic model of the transmission system.

The motion differential equations of the transmission of the lunar sampler are expressed as follows:

$$\mathbf{M}\ddot{\mathbf{q}} + \omega_c \mathbf{G}\dot{\mathbf{q}} + \left(\mathbf{K_b} + \mathbf{K_g} + \omega_c^2 \mathbf{K_\Omega}\right)\mathbf{q} = \mathbf{T} \tag{15}$$

In equation (15), $\mathbf{q}$ denotes the generalized coordinate array, $\mathbf{M}$ denotes the mass matrix, $\mathbf{G}$ denotes the gyro matrix, $\mathbf{K_b}$ denotes the bearing support stiffness matrix, $\mathbf{K_g}$ denotes the gear meshing stiffness matrix, $\mathbf{K_\Omega}$ denotes the centripetal stiffness matrix, and $\mathbf{T}$ denotes the force vector.

IV. NATURAL VIBRATION ANALYSIS OF THE TRANSMISSION AND EXPERIMENTAL VERIFICATION

A. NATURAL FRENQUENCY AND FORMATION

The differential equation of vibration for the transmission in the lunar surface sampler is as follows:

$$\left|\left(\mathbf{K_b} + \mathbf{K_g}\right) - \omega_i^2 \mathbf{M}\right| = 0 \tag{16}$$

Therefore, the form vector $\mathbf{\Phi_n}$ corresponding to the natural frequency n is satisfied as follows:

$$\mathbf{M}\ddot{\mathbf{\Phi}}_\mathbf{n} + \left(\mathbf{K_b} + \mathbf{K_g}\right)\mathbf{\Phi_n} = \mathbf{0} \tag{17}$$

In normal temperature conditions, the parameters of the transmission in the main driving component are shown in Table 1.

In the study, Runge–Kutta method is used to solve the dynamic model. In order to solve the model, a Matlab script is used, and the model is calculated by the ode45 solving module in Matlab. The system includes 36 degrees of freedom, and the natural frequencies are listed in Table 2.

As shown in Table 2, the system includes six pairs of double roots. They are f5 and f6, f10 and f11, f17 and f18, f22 and f23, f28 and f29, f31 and f32. Given the assumption that the geometric and physical parameters are identical, the repetition of the frequency phenomenon occurs and is caused by the symmetry of the planetary transmission system at all levels.

Eigenvectors corresponding to the natural frequencies are also obtained. Different eigenvectors reflect different modes of vibration. Based on the eigenvectors, vibration modes appear in the system and are shown in Table 3.

We can see that all the double roots appear in the translational and torsional vibration of high speed level. The formation vectors and formations corresponding to a few of the natural frequencies are shown in Table 4 and Figure 9, respectively. In figure 9, the dotted line represents the original position, and the solid line represents the position after the vibration.

B. EXPERIMENTAL STUDY OF THE INHERNET CHARACTERISTICS OF TRANSMISSION

In order to verify the correctness of the theoretical model and solution results, a vibration test platform is constructed based on the vibration table. The vibration test platform is shown in Figure 10.

Four acceleration sensors are used in the vibration experiments. Specifically, No. 1 and No. 2 denote control sensors and are pasted on the surface of the shaking table and platform, respectively, and No. 3 and No. 4 denote test sensors

TABLE 1. Parameters of each component in transmission.

	Parameter	Carrier	Sun gear	Planetary gear	Ring
I	Mass/g	35.93	15.41	12.60	103.48
	Moment of inertia/ $g\cdot mm^2$	35.93	7.7	6.27	99
	Tooth number	—	18	18	54
	Modulus	—	1	1	1
	Pressure angle / °	—	20	20	20
	Meshing stiffness / $N\cdot m^{-1}$	—	1.4×10^8	8×10^8	
	Bearing stiffness / $N\cdot m^{-1}$	8.22×10^8	7.54×10^8	6.59×10^8	8.55×10^8
	Tangential stiffness / $N\cdot m^{-1}$	—	—	—	2.6×10^{10}
II	Mass /g	85.55	21.44	15.31	103.48
	Moment of inertia / $g\cdot mm^2$	85.55	10.67	7.59	99
	Tooth number	—	18	18	54
	Modulus	—	1	1	1
	Pressure angle / °	—	20	20	20
	Meshing stiffness / $N\cdot m^{-1}$	—	1.7×10^8	1×10^9	
	Bearing stiffness / $N\cdot m^{-1}$	8.22×10^8	7.54×10^8	6.59×10^8	8.55×10^8
	Tangential stiffness / $N\cdot m^{-1}$	—	—	—	2.6×10^{10}

TABLE 2. Natural frequencies of transmission.

Order	1	2	3	4	5	6
Frequency/Hz	94.0	153.7	257.1	270.6	326.0	326.0
Order	7	8	9	10	11	12
Frequency/Hz	427.2	437.7	460.6	494.0	494.0	571.2
Order	13	14	15	16	17	18
Frequency/Hz	613.0	761.1	952.4	1057	1067	1067
Order	19	20	21	22	23	24
Frequency/Hz	1122	1135	1191	1354	1354	1358
Order	25	26	27	28	29	30
Frequency/Hz	1398	1415	1510	1651	1651	2192
Order	31	32	33	34	35	36
Frequency/Hz	2424	2424	2436	2482	3540	3665

TABLE 3. Vibration modes and natural frequencies.

Vibration mode	Natural frequency/Hz
Translational torsional vibration of high speed level	f5=326.09, f6=326.09, f10=494.04, f11=494.04, f17=1067.9,f18=1067.9, f22=1354.4, f23=1354.4, f28=1651.0, f29=1651.0, f31=2424.0, f32=2424.0
Translational torsional vibration of high speed level	f1=94.05, f3=257.19, f4=270.65, f8=437.74, f13=613.07, f20=1135.1, f25=1398.6, f33=2436.7
Translational torsional vibration of transmission system	f2=153.75, f7=427.24, f9=460.62, f12=571.25, f14=761.10,f15=952.49, f16=1057.4, f19=1122.1, f21=1191.1,f24=1358.7, f26=1415.8, f27=1510.8, f30=2192.6,f34=2482.4, f35=3540.5, f36=3665.0

that are pasted on the input and output of the transmission, respectively, to measure the vibration response of the high-speed sun gear and low-speed carrier.

Two sets of sine sweep experiments that exhibit different acceleration amplitudes were performed with respect to the transmission. The experimental conditions are listed in Table 5.

The test results of No. 3 and No. 4 sensors under the condition of acceleration amplitudes of 0.4 g and 0.8 g are shown in Figures 11 and 12, respectively.

Based on the experimental results, as shown in Figures 11 and 12, the natural frequencies of the two sets of sine sweep experiments are identical, and a difference only occurs in the amplitude of the response. Comparison results show that the experimental results are in good agreement with the calculation results, as shown in Table 6.

The vibration experiment verifies the accuracy of the theoretical model, and the model can be used to further investigate the mechanical response of the transmission during transportation.

V. MECHANICAL RESPONSE OF TRANSMISSION DURING THE TRANSPORTATION PROCESS

A. MECHANICAL ANALYSIS IN THE TRANSPORTATION PROCESS

The transmission is subjected to alternating impact, vibration, and acceleration from launching to landing. The aforementioned complicated and severe mechanical environments may cause damage to the transmission. We assume that the axial direction of the transmission is in the direction of z-axis, and the positive direction corresponds from the high-speed level to low-speed level. Given the symmetry of the system, we assume that the x-axis and y-axis are perpendicular to each other in the radial direction and satisfy the right-hand spiral rule.

In order to simulate and cover the mechanical environment during the transportation, in the study, sinusoidal vibration and random vibration are used to simulate the mechanical environment. The sine vibration mechanical conditions are listed in Table 7.

The vibration mechanical conditions in Table 5 and Table 6 are very harsh, and the laboratory doesn't have the corresponding test conditions. In the analysis of the inherent characteristics in the fourth section, the correctness of the model has been verified by experiments. Therefore, the dynamic

TABLE 4. Formation vectors corresponding to a few of the natural frequencies.

formation vectors	326.09 Hz(1)	326.09 Hz(2)	94.05 Hz	257.19 Hz	153.75 Hz	427.24 Hz
$x_s^{\mathrm{I}} / x_s^{\mathrm{II}}$	-0.1002/0	0.0128/0	0/-0.0030	0/0.2719	0/0	0/-0.0860
$y_s^{\mathrm{I}} / y_s^{\mathrm{II}}$	0.0445/0	0.1089/0	0/-0.0074	0/0.7196	0/0	0/-0.1213
$u_s^{\mathrm{I}} / u_s^{\mathrm{II}}$	0/0	0/0	0/-0.0027	0/-0.0012	0.4045/-0.0016	0.0108/0.0187
$\xi_1^{\mathrm{I}} / \xi_1^{\mathrm{II}}$	-0.5336/0	-0.1238/0	0/0.0030	0/0.0049	0.0045/0	0/0.0031
$\eta_1^{\mathrm{I}} / \eta_1^{\mathrm{II}}$	0.0256/0	0.3684/0	0/-0.3242	0/0.1884	-0.0276/0	0.0057/0.4652
$u_1^{\mathrm{I}} / u_1^{\mathrm{II}}$	-0.1910/0	-0.1533/0	0/-0.2676	0/-0.4388	-0.4460/0.0011	-0.0047/0.3091
$\xi_2^{\mathrm{I}} / \xi_2^{\mathrm{II}}$	0.2979/0	0.5125/0	0/0.0037	0/0.1293	0.0045/0	0/0.3410
$\eta_2^{\mathrm{I}} / \eta_2^{\mathrm{II}}$	0.3144/0	-0.1084/0	0/-0.3252	0/-0.1459	-0.0276/0	0.0057/-0.0203
$u_2^{\mathrm{I}} / u_2^{\mathrm{II}}$	0.0078/0	0.2086/0	0/-0.2807	0/0.2419	-0.4460/0.0012	-0.0047/-0.1396
$\xi_3^{\mathrm{I}} / \xi_3^{\mathrm{II}}$	0.2357/0	-0.3886/0	0/0.0030	0/-0.1341	0.0045/0	0/-0.3477
$\eta_3^{\mathrm{I}} / \eta_3^{\mathrm{II}}$	-0.3399/0	-0.2600/0	0/-0.3254	0/-0.1388	-0.0276/0	0.0057/-0.0360
$u_3^{\mathrm{I}} / u_3^{\mathrm{II}}$	0.1831/0	-0.0553/0	0/-0.2807	0/0.1452	-0.4460/0.0012	-0.0047/-0.3604
$x_r^{\mathrm{I}} / x_r^{\mathrm{II}}$	-0.1720/0	-0.0990/0	0/0	0/0.0188	0/0	0/-0.1168
$y_r^{\mathrm{I}} / y_r^{\mathrm{II}}$	-0.0503/0	0.1493/0	0/0	0/-0.0516	0/0	0/0.3209
$u_r^{\mathrm{II}} / u_r^{\mathrm{II}}$	0/0	0/0	0/-0.5897	0/0.0243	-0.4871/0	0/-0.1197
$x_c^{\mathrm{I}} / x_c^{\mathrm{II}}$	-0.4906/0	-0.1138/0	0/0	0/0.0035	0/0	0/-0.0021
$y_c^{\mathrm{I}} / y_c^{\mathrm{II}}$	0.0331/0	0.4784/0	0/0	0/0.1430	0/0	0/0.3291
$u_c^{\mathrm{I}} / u_c^{\mathrm{II}}$	0/0	0/0	0/-0.3258	0/-0.0357	-0.0081/0	0.0044/0.1945

model above will be used to analyze the response during transportation in this section.

The random vibration mechanical conditions are listed in Table 8.

B. EXCITATION MODEL AND RESPONSE CALCULATION OF SINUSOIDAL VIBRATION

The sine vibration excitation function satisfies the following conditions:

$$y(t) = A \sin \omega t \tag{18}$$

$$\dot{y}(t) = A\omega \cos \omega t = v \cos \omega t \tag{19}$$

$$\ddot{y}(t) = -A\omega^2 \sin \omega t = -a \sin \omega t \tag{20}$$

The relationship between octave frequency, scanning speed, lower limit frequency, and time in the sine vibration is shown in equation (21) as follows:

$$f = f_l \cdot 2^{\frac{n_s t}{60}} \tag{21}$$

Based on the above analysis, the mathematical model corresponding to the mechanical conditions in Table 6 is as follows:

$$a(t) = \begin{cases} 0.073 \cos(10\pi \times 2^{t/30}t) \\ \times \left[\dfrac{(\log 2)^2}{90} \times 2^{t/30}t + \dfrac{2 \log 2}{3} \times 2^{t/30} \right] \\ -0.228 \sin(10\pi \times 2^{t/30}t) \\ \times \left[\dfrac{\log 2}{3} \times 2^{t/30}t + 10 \times 2^{t/30} \right]^2, \\ \qquad\qquad 0 \le t < 47.55s \\ 21g \cdot \sin(10\pi \times 2^{t/30}t), \quad 47.55 \le t < 95.10s; \\ 30g \cdot \sin(10\pi \times 2^{t/30}t), \quad 95.10 \le t < 120s; \\ 15g \cdot \sin(10\pi \times 2^{t/30}t), \quad 120 \le t < 129.66s \end{cases} \tag{22}$$

We replace equation (22) in the program written in Matlab, and the response of each component under the mechanical

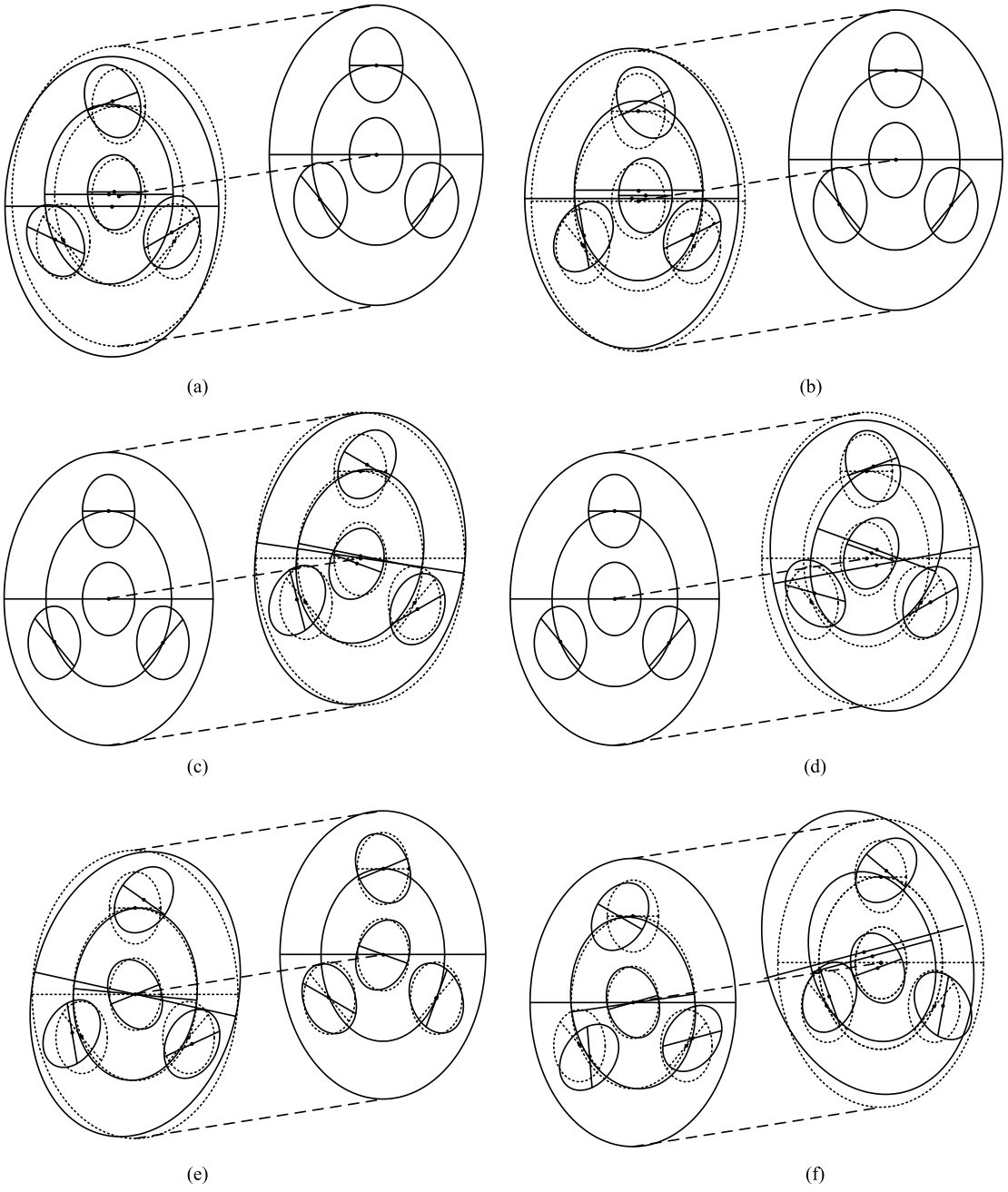

FIGURE 9. Formations corresponding to a few of the natural frequencies. (a) Formation of frequency f5. (b) Formation of frequency f6. (c) Formation of frequency f1. (d) Formation of frequency f3. (e) Formation of frequency f2. (f) Formation of frequency f7.

condition is obtained. The vibration displacement response in the ξ direction and η direction of high-speed planetary gear and low-speed planetary gear are shown in Figures 13 and 14, respectively.

Based on the above analysis, the responses of the sun gear, carrier, and inner gear in the x direction are almost zero. The planetary gear exhibits significant displacements in two radial directions. With respect to the three planetary gears at the same level, the response is almost identical along the ξ direction and η direction.

C. EXCITATION MODEL RESPONSE CALCULATION OF RANDOM VIBRATION

Based on the mechanical conditions of random vibration, as shown in Table 6, the relation between power spectral density and frequency is given in equation (23) as follows:

$$W_a(f) = \begin{cases} 0.002 \times 3.98^{\log_2 \frac{f}{20}} & 20 \le f < 200 \\ 0.2 & 200 \le f \le 2000 \end{cases} \quad (23)$$

We replace equation (23) in the program written in Matlab, and the response of each component under the mechanical

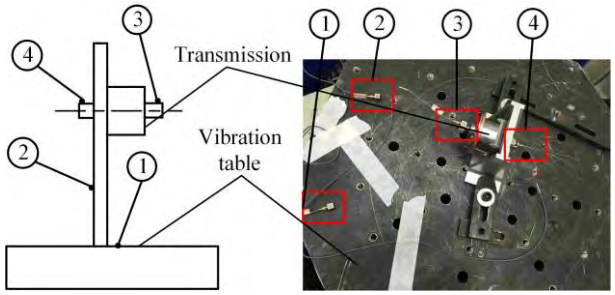

FIGURE 10. Vibration test platform of transmission. (a) Schematic. (b) Sensor stickup positions.

TABLE 5. Experimental conditions of the sine sweep.

Project	Acceleration amplitude/ (g)	Frequency range/ (Hz)	Frequency sweep speed/ (oct/min)
Test 1	0.4	5–1500	4
Test 2	0.8	5–1500	4

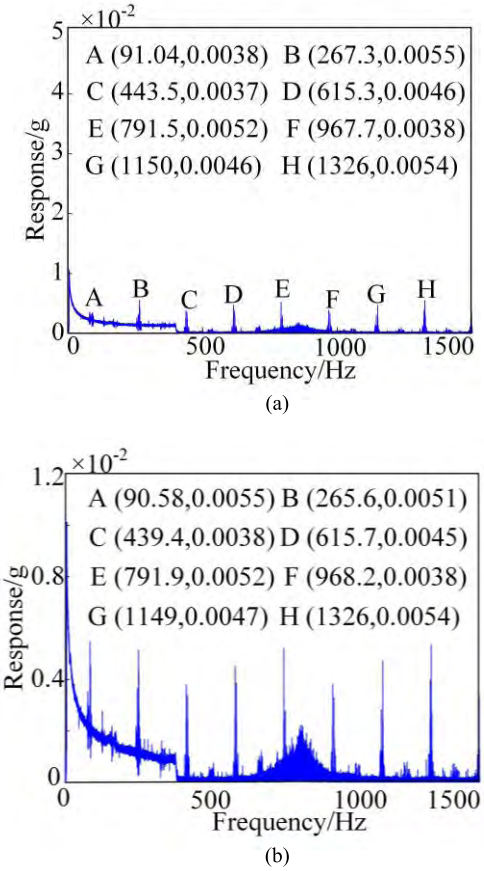

FIGURE 11. Results of 0.4 g acceleration amplitude. (a) Test results of sensor No.3. (b) Test results of sensor No.4.

condition is obtained. The power spectral density in the ξ direction and η direction of high-speed planetary gear and low-speed planetary gear are shown in Figures 15 and 16, respectively.

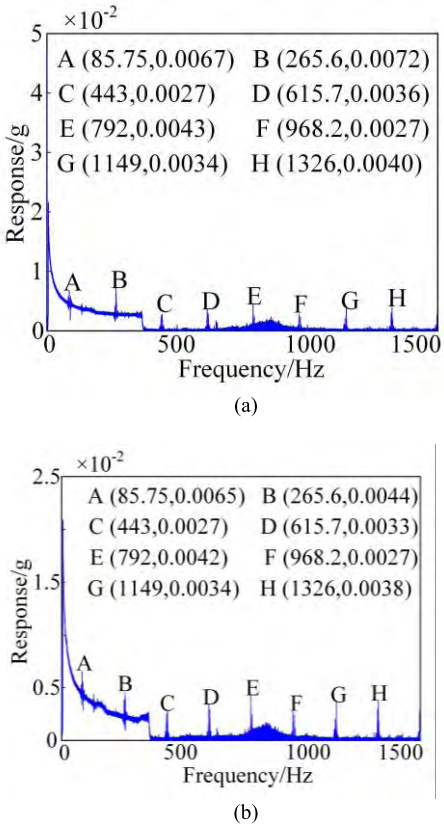

FIGURE 12. Results of 0.8 g acceleration amplitude. (a) Test results of sensor No.3. (b) Test results of sensor No.4.

TABLE 6. Comparison between theoretical and experimental values.

Theoretical values/ (Hz)	Experimental values/ (Hz)	Theoretical values/ (Hz)	Experimental values/ (Hz)
94.0	91.04	270.6	267.3
437.7	443.5	613.0	615.3
761.1	791.5	952.4	967.7
1135	1150	1354	1326

TABLE 7. Sine vibration mechanical conditions.

Test direction	Frequency range/ (Hz)	Displacement/ (mm)	Acceleration/ (g)	Frequency sweep speed/ (oct/min)
y-axis direction	5–15	23.17		2
	15–45		21	
	45–80		30	
	80–100		15	

Based on the above analysis, although the external load is in the y direction, the vibration responses of each component in the x direction are of equal magnitude owing to system resonance. Given the characteristic of each component, several components exhibit different amplitude responses, and there are differences in the frequency that causes the maximum response of each component.

According to the calculation results of all the parts in the transmission, the structure can stand the mechanical vibration in the process of transportation.

TABLE 8. Random vibration mechanical conditions.

Test direction	Frequency range/ (Hz)	Power spectral density/ Slope	Total root mean square acceleration	Test time/(min)
y-axis direction	20–200 200–2000	+6 dB/oct 0.2 g^2/Hz	19.3 g	2

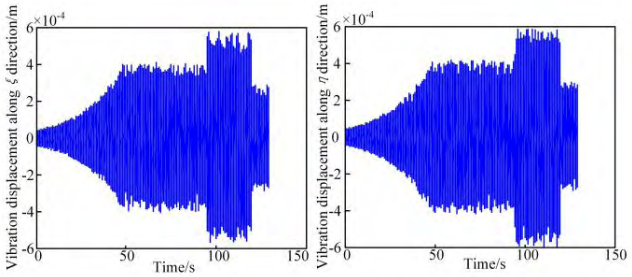

FIGURE 13. Vibration displacement response of high-speed planetary gear.

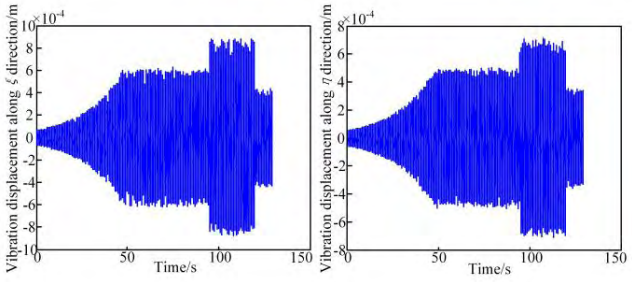

FIGURE 14. Vibration displacement response of low-speed planetary gear.

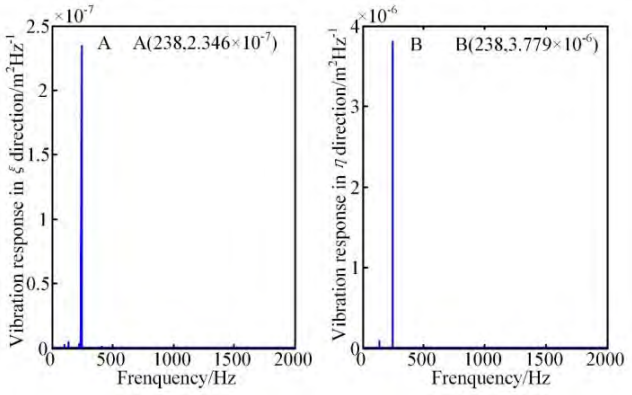

FIGURE 15. Response of high-speed planetary gear.

VI. LOAD SHARING CHARACTERISTIC ANALYSIS OF TRANSMISSION

The load of each planet gear is not uniform because of the deformation, manufacturing, and installation errors of parts including the planetary gear, sun gear, and carrier. Thus, the carrying capacity and service life of the planetary gears could be lower than the expected value. The environmental conditions of lunar surface are complex; further, a wide range of temperature changes increase the error value of each part [22], [23]. In this study, static and dynamic

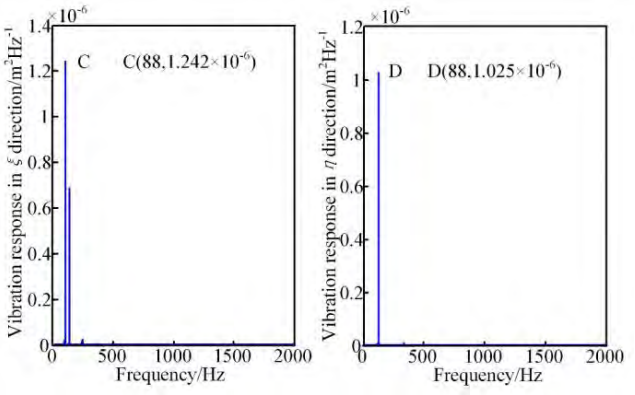

FIGURE 16. Response of low-speed planetary gear.

load sharing characteristics are examined. Various errors are directly introduced into the static analysis, and the results are more evident. The dynamic analysis considers inertia and time-varying mesh stiffness of each component; the results are more realistic.

A. ANALYSIS OF STATIC LOAD SHARING CHARACTERISTICS

When the transmission rotates at a fixed speed, the influence of damping, time-varying mesh stiffness, and bearing stiffness is neglected. This model is termed as the static system model. The error for a transmission mainly includes floating meshing error and manufacturing and installation errors.

The integrated meshing error is expressed as follows:

$$\Delta_{spi} = e_{spi} + \Delta_{si} + \Delta_{cis} \tag{24}$$

$$\Delta_{rpi} = e_{rpi} + \Delta_{ri} + \Delta_{cir} \tag{25}$$

Relative displacement of planetary gear and sun gear with integrated meshing error and that of planetary gear and sun gear with integrated meshing error are given in equation (26) as follows:

$$\begin{cases} \delta_{sie} = \delta_{si} - \Delta_{spi} = x_s \sin\psi_{si} - y_s \cos\psi_{si} \\ \quad - u_s + x_i \sin\alpha + y_i \cos\alpha - u_i - \Delta_{spi} \\ \delta_{rie} = \delta_{ri} - \Delta_{rpi} = x_r \sin\psi_{ri} - y_r \cos\psi_{ri} \\ \quad - u_r - x_i \sin\alpha + y_i \cos\alpha + u_i - \Delta_{rpi} \end{cases} \tag{26}$$

The load of the external gear and internal gear on the meshing line are expressed in equations (27) and (28), respectively, as follows:

$$W^j_{spi} = k^j_{si}\delta^j_{sie} = k^j_{si}(\delta^j_{si} - \Delta^j_{spi}) \tag{27}$$

$$W^j_{rpi} = k^j_{ri}\delta^j_{rie} = k^j_{ri}(\delta^j_{ri} - \Delta^j_{rpi}) \tag{28}$$

With respect to each level, the following static equilibrium equations are applicable:

$$\sum_{i=1}^{3} W^j_{spi} r^j_{bs} = T^j_s \tag{29}$$

$$W^j_{rpi} = W^j_{spi} \tag{30}$$

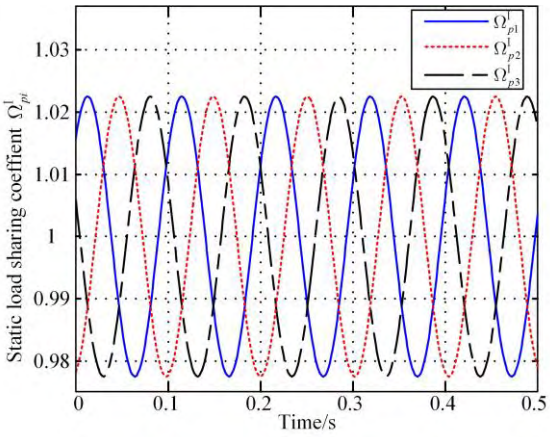

FIGURE 17. Static load sharing coefficient of high-speed level.

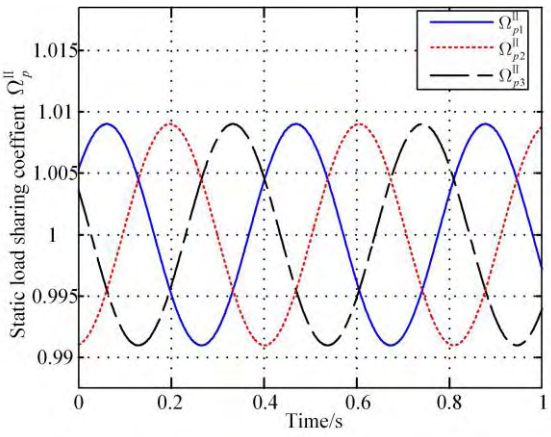

FIGURE 18. Static load sharing coefficient of low-speed level.

Therefore, the static load sharing coefficient of No, i planet gear in level j is as follows:

$$\Omega_i^j = W_{spi}^j \cdot (3r_{bs}^j)/T_s^j \tag{31}$$

It is assumed that the eccentric error of each gear is 10 μm and the input speed is 7680 rpm. The static load sharing coefficient of each planetary gear is shown in Figures 17 and 18.

Static load sharing coefficient of the high-speed level is 1.023 and that of the low-speed level is 1.0091. The static model is a simplified form of the dynamic model, and the analytical solution is obtained by calculations. The main contradiction of the system is evident by using a static-based model.

B. ANALYSIS OF DYNAMIC LOAD SHARING CHARACTERISTICS

$$F_{si}^{\mathrm{I}}(t) = k_{si}^{\mathrm{I}}(t) \cdot \delta_{sie}^{\mathrm{I}} \tag{32}$$

$$F_{ri}^{\mathrm{I}}(t) = k_{ri}^{\mathrm{I}}(t) \cdot \delta_{rie}^{\mathrm{I}} \tag{33}$$

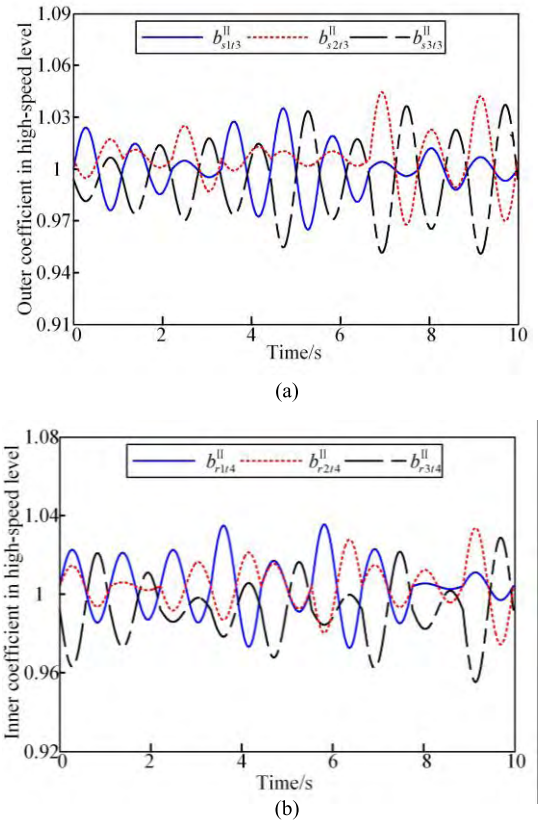

FIGURE 19. Dynamic load sharing coefficient of high-speed level. (a) High-speed outer meshing. (b) High-speed inner meshing.

The dynamic load sharing coefficient in a meshing cycle are as follows:

$$b_{sit1}^{\mathrm{I}} = 3 \cdot (F_{sit1}^{\mathrm{I}}(t))_{\max} \Big/ \sum_{i=1}^{3} (F_{sit1}^{\mathrm{I}}(t))_{\max} \tag{34}$$

$$b_{rit2}^{\mathrm{I}} = 3 \cdot (F_{rit2}^{\mathrm{I}}(t))_{\max} \Big/ \sum_{i=1}^{3} (F_{rit2}^{\mathrm{I}}(t))_{\max} \tag{35}$$

Dynamic load sharing coefficient of the outer meshing and inner meshing are given in equations (36) and (37), respectively, as follows:

$$\Pi_{si}^{\mathrm{I}} = \left| b_{sit1}^{\mathrm{I}} - 1 \right|_{\max} + 1 \tag{36}$$

$$\Pi_{ri}^{\mathrm{I}} = \left| b_{rit2}^{\mathrm{I}} - 1 \right|_{\max} + 1 \tag{37}$$

The dynamic load sharing coefficient curve of each planetary gear is shown in Figures 19 and 20.

Based on the aforementioned curves, the dynamic load sharing coefficient of each planetary gear in the high-speed level includes $\Pi_{s1}^{\mathrm{I}} = 1.056$, $\Pi_{s2}^{\mathrm{I}} = 1.065$, $\Pi_{s3}^{\mathrm{I}} = 1.047$, $\Pi_{r1}^{\mathrm{I}} = 1.033$, $\Pi_{r2}^{\mathrm{I}} = 1.044$, and $\Pi_{r3}^{\mathrm{I}} = 1.063$. The dynamic load sharing coefficient of each planetary gear in the low-speed level includes $\Pi_{s1}^{\mathrm{II}} = 1.034$, $\Pi_{s2}^{\mathrm{II}} = 1.044$, $\Pi_{s3}^{\mathrm{II}} = 1.052$, $\Pi_{r1}^{\mathrm{II}} = 1.036$, $\Pi_{r2}^{\mathrm{II}} = 1.032$, and $\Pi_{r3}^{\mathrm{II}} = 1.045$. Therefore, the dynamic load sharing coefficient of the

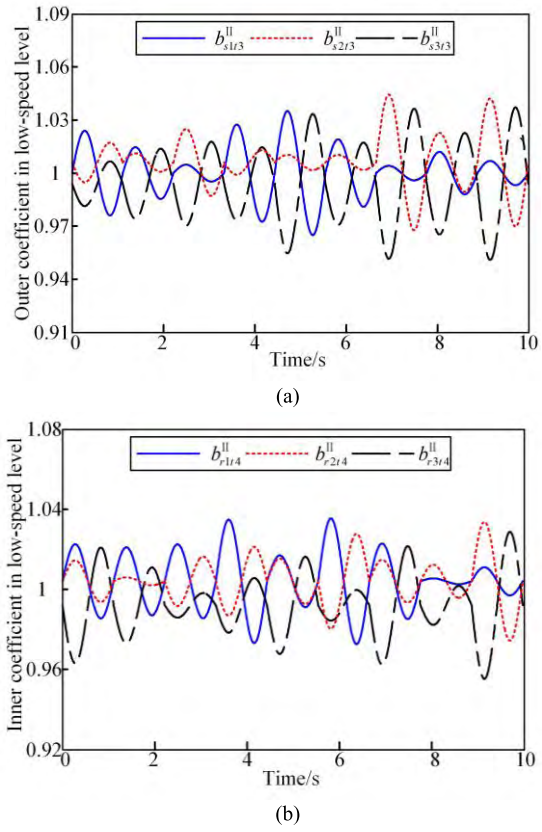

FIGURE 20. Dynamic load sharing coefficient of low-speed level. (a) Low-speed outer meshing. (b) Low-speed inner meshing.

high-speed level is $\Pi^{\mathrm{I}} = 1.065$, and that of the low-speed level is $\Pi^{\mathrm{II}} = 1.052$.

VII. CONCLUSION

The uncertainty of the soil on the moon and the harsh mechanical environment during transportation have a great impact on the transmission, and they also influence the completion of the sampling task. In this study, a translational torsional dynamic model is established, based on Runge-Kutta method, the inherent characteristics of the transmission is obtained, and the corresponding verification experiments are also carried out. Sinusoidal vibration and random vibration are used to simulate the mechanical environment. The experimental conditions are modeled and replaced in the kinetic equations. The static and dynamic load sharing characteristics are obtained considering floating meshing error, manufacturing and installation errors. The conclusions are as follows:

1) In previous studies, most scholars studied the single stage gear system. In this paper, the inherent characteristics, loading characteristics, and transportation mechanical response of two stage gear system were studied, and the corresponding experimental verification was carried out.
2) In the analysis of inherent characteristics, there are 6 pairs of double roots. Many kinds of formations occur, including translation, torsion and coupling of them. In the corresponding verification experiments, the calculation results and experimental results are in good agreement. The theoretical model is verified by the experiments.
3) In the results of sinusoidal vibration, the responses of sun gear, carrier and inner gear in x direction are almost zero, the planetary gear has significant displacements in the two radial directions. In the results of random vibration, the vibration response of each component in the x direction are of equal magnitude.
4) Static load sharing coefficient of high-speed level is $\Omega^{\mathrm{I}} = 1.023$, and that of low-speed level is $\Omega^{\mathrm{I}} = 1.0091$. Dynamic load sharing coefficient of high-speed level is $\Pi^{\mathrm{I}} = 1.065$, and that of low-speed level is $\Pi^{\mathrm{I}} = 1.052$. The load sharing coefficient of high-speed level is higher than that of low-speed level.

Inherent characteristics, load sharing characteristics and transportation mechanical response of transmission system are studied in this paper. The study may contribute to parameter setting and structural design in a lunar exploration project.

REFERENCES

[1] R. G. Parker, V. Agashe, and S. M. Vijayakar, "Dynamic response of a planetary gear system using a finite element/contact mechanics model," *J. Mech. Des.*, vol. 122, no. 3, pp. 304–310, Mar. 2000.
[2] P. Sondkar and A. Kahraman, "A dynamic model of a double-helical planetary gear set," *Mechanism Mach. Theory*, vol. 70, pp. 157–174, Dec. 2013.
[3] A. Singh, "Application of a system level model to study the planetary load sharing behavior," *J. Mech. Des.*, vol. 127, no. 3, pp. 469–476, 2003.
[4] J. X. Zhou, W. Sun, and L. Yuan, "Nonlinear vibroimpact characteristics of a planetary gear transmission system," *Shock Vib.*, vol. 2016, Nov. 2016, Art. no. 4304525.
[5] H. Wang, T. Zhang, G. Liu, and L. Wu, "System-structure coupling dynamic analysis of planetary gears," *Math. Problems Eng.*, vol. 2015, May 2015, Art. no. 350616.
[6] S. D. Yavuz, Z. B. Saribay, and E. Cigeroglu, "Nonlinear time-varying dynamic analysis of a spiral bevel geared system," *Nonlinear Dyn.*, vol. 92, no. 4, pp. 1901–1919, 2018.
[7] T. Eritenel and R. G. Parker, "Modal properties of three-dimensional helical planetary gears," *J. Sound Vib.*, vol. 325, nos. 1–2, pp. 397–420, 2009.
[8] Y. Guo and R. G. Parker, "Purely rotational model and vibration modes of compound planetary gears," *Mechanism Mach. Theory*, vol. 45, no. 3, pp. 365–377, 2010.
[9] D. R. Kiracofe and R. G. Parker, "Structured vibration modes of general compound planetary gear systems," *J. Vib. Acoust.*, vol. 129, no. 1, pp. 1–16, 2007.
[10] X. Wu and R. G. Parker, "Vibration of rings on a general elastic foundation," *J. Sound Vibrat.*, vol. 295, nos. 1–2, pp. 194–213, 2006.
[11] Y. C. Guo and R. G. Parker, "Sensitivity of general compound planetary gear natural frequencies and vibration modes to model parameters," *J. Vib. Acoust.*, vol. 132, no. 1, pp. 1–13, 2010.
[12] J. Wang, D. Qin, and Y. Ding, "Dynamic behavior of wind turbine by a mixed flexible-rigid multi-body model," *J. Syst. Des. Dyn*, vol. 3, no. 3, pp. 403–419, 2009.
[13] S. Zhou, Z. Ren, G. Song, and B. Wen, "Dynamic characteristics analysis of the coupled lateral-torsional vibration with spur gear system," *Int. J. Rotating Machinery*, vol. 2015, Sep. 2015, Art. no. 371408.
[14] V. K. Ambarisha and R. G. Parker, "Suppression of planet mode response in planetary gear dynamics through mesh phasing," *J. Vib. Acoust.*, vol. 128, no. 2, pp. 133–142, 2006.
[15] R. G. Parker and J. Lin, "Mesh phasing relationships in planetary and epicyclic gears," *J. Mech. Des.*, vol. 126, no. 2, pp. 365–370, 2004.
[16] A. N. Montestruc, "Influence of planet pin stiffness on load sharing in planetary gear drives," *J. Mech. Des.*, vol. 133, no. 1, pp. 014501-1–014501-7, 2011.

[17] A. Bodas and A. Kahraman, "Influence of carrier and gear manufacturing errors on the static load sharing behavior of planetary gear sets," *Int. J. C, Mech. Syst., Mach. Elements Manuf.*, vol. 47, no. 3, pp. 908–915, 2004.
[18] H. Ligata, A. Kahraman, and A. Singh, "A closed-form planet load sharing formulation for planetary gear sets using a translational analogy," *J. Mech. Des.*, vol. 131, no. 2, p. 021007, 2009.
[19] L. Hong, Y. Qu, and Y. Tan, "Vibration based diagnosis for planetary gearboxes using an analytical model," *Shock Vib.*, vol. 2016, Oct. 2016, Art. no. 2620518.
[20] X. Shuiqing, Z. Ke, C. Yi, H. Yigang, and F. Li, "Gear fault diagnosis in variable speed condition based on multiscale chirplet path pursuit and linear canonical transform," *Complexity*, vol. 2018, Feb. 2018, Art. no. 3904598.
[21] W. Yu, C. K. Mechefske, and M. Timusk, "A new dynamic model of a cylindrical gear pair with localized spalling defects," *Nonlinear Dyn.*, vol. 91, no. 4, pp. 2077–2095, 2017.
[22] H. Xiao, D. Tang, Z. Deng, C. Li, F. Kong, and S. Jiang, "Thermal analysis and experimental verification of the transmission in a lunar drilling system," *Appl. Therm. Eng.*, vol. 113, no. 1, pp. 765–773, 2017.
[23] D. Tang, H. Xiao, F. Kong, Z. Deng, S. Jiang, and Q. Quan, "Thermal analysis of the driving component based on the thermal network method in a lunar drilling system and experimental verification," *Energies*, vol. 10, no. 3, pp. 355-1–355-17, 2017.

HONG XIAO received the B.S. degree in mechanical engineering from Yanshan University, Qinhuangdao, China, in 2011, and the M.S. degree in mechanical engineering from the Harbin Institute of Technology, Harbin, China, in 2013, where he is currently pursuing the Ph.D. degree with the School of Mechatronics Engineering. His research interests include thermal analysis and dynamic analysis of transmission systems.

DEWEI TANG received the master's and Ph.D. degrees in mechanical engineering from the Harbin Institute of technology, Heilongjiang, China, in 1991 and 2000, respectively. Since 2005, he has been a Professor with the School of Mechatronics Engineering, Harbin Institute of Technology. He has authored or co-authored over 70 articles, and he holds nine patents. Since 2010, he has been participating with the third phase project of the Chinese lunar exploration. He is currently involved in two main research projects: drilling and sampling on the moon and near-earth asteroid sample return. His research interests principally include drilling performance analyses and enhancement in extreme environments and undisturbed sampling technique.

ZONGQUAN DENG received the B.S. and M.S. degrees in mechanical engineering from the School of Mechatronics Engineering, Harbin Institute of Technology, Harbin, China, in 1982 and 1984, respectively. He is currently a Research Director with the Aerospace Mechanism and Control Research Team, Harbin Institute of Technology. Since 2017, he has been an Academician of the China Engineering Academy. He has more than 30 years designing and manufacturing experiences in aerospace system and advanced robotics. In recent years, he has been involved in the Chinese Lunar Exploration Program. He has author of three books, more than 400 articles, and more than 50 inventions.

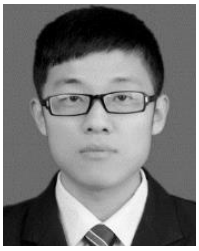

CHUANYANG LI received the B.S. degree in mechanical engineering from Yantai University, Yantai, China, in 2014, and the M.S. degree in mechanical engineering from the Harbin Institute of Technology, Harbin China, in 2016, where he is currently pursuing the Ph.D. degree with the School of Mechatronics Engineering. His research interests include multi-loop coupled mechanisms, variable geometry truss, and screw theory.

SHENGYUAN JIANG received the B.S. degree in mechanical metallurgy from the North China University of Technology, Beijing, China, in 1992, and the M.S. and Ph.D. degrees in mechanical design and theory from the School of Mechatronics Engineering, Harbin Institute of Technology, Harbin, China, in 1998 and 2001, respectively. Since 2011, he has been a Professor with the Department of Manufacturing Engineering for Aviation and Aerospace, Harbin Institute of Technology. His current research interests include planetary penetration, drilling and sampling techniques, aerospace system design, optimization, and simulation.